

# Nonlinear Optical Imaging of Carrier Transport at the Semiconductor-Insulator Interface in Organic Field-Effect Transistors

Payal Bhattacharya<sup>1</sup>, Ping Yu, and Suchismita Guha<sup>1\*</sup>

*Department of Physics and Astronomy, University of Missouri, Columbia, Missouri 65211, USA*

 (Received 28 January 2023; revised 14 March 2023; accepted 29 March 2023; published 20 April 2023)

Organic field-effect transistors (FETs) are witnessing a revolution in their performance, in part, due to a reduction in contact resistance, and through controlled morphology of the organic semiconducting film. Another major consideration is the role of the dielectric layer in dictating transport properties. The transient electric-field-induced second-harmonic generation (EFISHG) technique allows visualization of carrier dynamics in the channel region of a FET by capturing the movement of the induced dielectric polarization. A microscopic imaging system using a broadband femtosecond laser and a pulse compensation arrangement is constructed for imaging transient EFISHG from organic FETs by synchronized laser and voltage pulses. By varying the dielectric layer in organic FETs comprising pentacene and a donor-acceptor conjugated polymer as semiconducting layers, we show that EFISHG images provide an accurate estimate of the carrier mobility along with providing insights into channel formation and the electric field distribution within the channel region. We further correlate the interface charging effects observed in EFISHG to the interface trap density obtained by capacitance-voltage and conductance-voltage from metal-insulator-semiconductor diodes.

DOI: [10.1103/PhysRevApplied.19.044059](https://doi.org/10.1103/PhysRevApplied.19.044059)

## I. INTRODUCTION

Although organic transistors have seen a significant increase in their device performance in recent years [1–5], they have yet to achieve the same status as inorganic MOSFETs in integrated circuits. Organic field-effect transistors (FETs) still struggle with low carrier mobility and speed. In addition to the device architecture parameters in organic FETs, the transport mechanism in organic semiconductors is inherently limited by several factors, typically due to a hopping mechanism of carriers across localized states [6]. This is primarily the reason for lower carrier mobilities in organic FETs compared to MOSFETs. Furthermore, since organic FETs mainly operate in the accumulation region, the metal-semiconductor interface plays a large role in their performance. Similarly, the dielectric-semiconductor interface dictates the formation of the accumulation region. Polarizable polymer gate dielectrics often broaden the density of states (DOS) at the semiconductor-dielectric interface, lowering carrier mobilities due to localization effects [7]. Electrical measurements fail to provide detailed insights as to why the same semiconductor with different dielectric interfaces in organic FETs may yield different carrier mobilities and other device parameters. In this quest, nonlinear optical methods based on second-harmonic generation (SHG)

were instrumental for probing interfaces of Si and other semiconductors more than 40 years ago, where the inversion symmetry could be broken due to inhomogeneity [8, 9]. Since SHG inherently depends on noncentrosymmetric systems, the application of an electric field is a mechanism of breaking the symmetry. Electric-field-induced SHG (EFISHG) provided a powerful method for the observation of Si-SiO<sub>2</sub> buried interfaces by the application of an external dc electric field in the 1990s, and is an effective way of mapping the interface charge distribution in metal-oxide-semiconductor (MOS) devices [10–14]. The technique has also been applied for probing CMOS integrated circuits [15].

Manaka, Iwamoto, and co-workers pioneered EFISHG techniques for application in organic FETs [16–20]. The operation of such FETs relies on the injection of carriers from the electrodes, trapping of carriers, and formation of an accumulation layer at the semiconductor-dielectric interface. Time-resolved EFISHG, in particular, has been a powerful tool for investigating carrier propagation, which is dependent on the interfacial condition of the channel formed at the dielectric-semiconductor interface [21]. In this method, the frequency of the pulsed voltage applied to the device matches the repetition rate of the pulsed-laser light. The time delay between the two signals (voltage and the laser pulse) gives a snapshot of the distribution of the injected carriers. Based on the Maxwell-Wagner and a drift-diffusion model, the displacement of the dielectric

\* guhas@missouri.edu

polarization yields the carrier mobility [22]. The carrier mobility extracted from transient EFISHG measurements does not suffer from contact resistance effects unlike steady-state current-voltage characteristics, which suffer from the contact resistance at the interface between the electrodes and the organic film. Further, transient EFISHG images help visualize the transport of carriers across the FET channel.

EFISHG techniques accurately map the electric field in the device channel and provide insight into the mobile charge distribution as well as interface and bulk trapped charge distribution in the semiconductor and dielectric layers. Since the method is sensitive to both mobile and trapped charges, it is valuable for monitoring carrier dynamics in both semiconducting and dielectric materials [23].

Here, we explore EFISHG imaging from organic FETs comprising different semiconductor-dielectric interfaces. Not only do the EFISHG images provide real-time measurement of the carrier dynamics in organic FETs, but they also reveal the impact of the semiconductor-dielectric interface to the mechanism of transport. Pentacene and a donor-acceptor copolymer (DPP-DTT) with the donor moiety of dithienylthieno[3,2-b]thiophene (DTT) and an acceptor moiety of *N*-alkyl diketopyrrolopyrrole (DPP) are used as model semiconducting layers for a small molecule versus a solution processable polymer along with various polymeric and oxide dielectric layers. We discuss the EFISHG imaging setup in Sec. II C involving a prism compressor for minimizing the group-velocity dispersion of the femtosecond (fs) pulse. Time-resolved EFISHG (TR EFISHG) images are obtained by synchronizing an ultrafast laser pulse (100 fs) of repetition rate 1 kHz with a pulsed voltage applied to the FET and by changing the delay between the two signals. Section III provides three different cases where TR EFISHG images are obtained. In the first case, the FETs are under normal operating condition with the application of both drain-source and gate-source voltages. Changing the delay between the laser pulse and the applied voltage helps discern the movement of the carriers in terms of an induced polarization wave front from the source to the drain contact. This indirectly provides a mechanism for obtaining the FET carrier mobility without the effect of any contact resistance and the impact of traps. In the second case, only a gate-source voltage is applied, which allows for charge injection without any drift source-drain current. These images highlight the effect of interface charging. To account for the differences in the interface charging phenomena observed in pentacene and DPP-DTT FETs (with the same dielectric layer), we conduct detailed capacitance and conductance measurements from equivalent metal-insulator-semiconductor (*M-I-S*) diodes. A slightly higher interface trap density and a higher carrier concentration in DPP-DTT compared with pentacene are responsible for the fast formation of the

accumulation layer as evinced by the EFISHG images, and further agrees with the Maxwell-Wagner model. The last case highlights the application of only a source-drain potential to the FETs, which results in the phenomenon of EFISHG without any carrier propagation. Such images help map the voltage within the channel region.

## II. EXPERIMENTAL DETAILS

### A. Materials and device fabrication

Pentacene and the DPP-DTT copolymer are procured through Tokyo Chemical Industry and 1-Material Inc. (Dorval, Quebec, Canada), respectively.  $\text{Si}^{++}/\text{SiO}_2$  and glass substrates are obtained from WaferPro Inc. and Fisher Scientific Inc., respectively. The gold wire (Au wire, 99.99% pure) used for thermal evaporation of the electrodes are obtained from Kurt J. Lesker Inc. Poly(4-vinylphenol) (PVP) ( $M_w = 25\,000$ ) and crosslinking agent poly(melamine-co-formaldehyde) methylated (PMMF) (84 wt% in 1-butanol), and poly (methyl methacrylate) (PMMA) are purchased from Sigma Aldrich. Other solvents such as propylene glycol monomethyl ether acetate (PGMEA), *N,N*-dimethylformamide (DMF) and dimethyl sulfoxide (DMSO) are also obtained from Sigma Aldrich.

Four different bottom-gate, top-contact (BGTC) geometry organic FETs are used in this investigation. In the  $\text{Si}^{++}/\text{SiO}_2$  wafers, a 525- $\mu\text{m}$ -thick  $\text{Si}^{++}$  layer served as the gate electrode and a 200-nm-thick  $\text{SiO}_2$  served as the gate dielectric. The polymer dielectrics are spin coated on a 50-nm-thick vacuum evaporated Al layer that is deposited on plasma-treated glass slides. The evaporation chamber pressure is at  $3 \times 10^{-5}$  mbar with a steady deposition rate of 1  $\text{\AA}/\text{s}$  for Al deposition. Two different polymer dielectrics are subsequently used as gate dielectrics. The PMMA is dissolved in DMSO with 60-mg/ml concentration. The solution is subsequently placed on a hot plate at 130  $^\circ\text{C}$  with a magnetic stirrer for 1 h. The films are spin coated on the Al-coated glass slides at 5000 rpm for 60 s and then vacuum annealed at 100  $^\circ\text{C}$  for 1 h. The film thickness is approximately 150 nm. The second dielectric is cross-linked poly-4-vinyl phenol (cPVP). PVP and PMMF, serving as the cross-linking agent, are diluted with PGMEA to prepare 80-mg/ml cPVP solution. The solution is heated at 80  $^\circ\text{C}$  for 1 h and magnetically stirred overnight. The solution is then spin coated onto the glass slides using the same recipe as the PMMA. The films are subsequently annealed under vacuum at 180  $^\circ\text{C}$  for 1 h. These films had a thickness of 130 nm.

The semiconductors are deposited either on  $\text{SiO}_2$  or on polymer dielectrics. Pentacene is thermally evaporated with a thickness of 50 nm while maintaining an evaporation pressure below  $3 \times 10^{-5}$  mbar and a steady deposition rate of 0.3  $\text{\AA}/\text{s}$ . 5 mg/ml solution of DPP-DTT is prepared in dichlorobenzene and the solution is heated in three steps: (i) 100  $^\circ\text{C}$  for 1 h, (ii) 130  $^\circ\text{C}$  for 2-3 h, and (iii) 150  $^\circ\text{C}$  for

2 h. It is magnetically stirred overnight. The solution is then spin coated on the substrates at 900 rpm for 60 s. The films are vacuum annealed at 120 °C for 1 h. The source and drain gold electrodes are deposited by thermal evaporation on top of the active layer with 50 nm thickness using a shadow mask. Each substrates had four FETs with channel width of 1000  $\mu\text{m}$  and channel length of 50  $\mu\text{m}$ , 75  $\mu\text{m}$ , 100  $\mu\text{m}$ , and 125  $\mu\text{m}$ . All TR EFISHG experiments are carried out with the 50- $\mu\text{m}$  channel length FET. The  $M$ - $I$ - $S$  diodes are fabricated using the thickness of the semiconductor and dielectric layer as the FETs.

### B. Electrical characterization

The electrical characterization of the FETs is conducted using Keithley sourcemeters 236 and 2400 controlled by a LabVIEW program. The capacitance-voltage ( $C$ - $V$ ) and conductance-voltage ( $G$ - $V$ ) measurements are carried out using a precision HP 4284 LCR operated by a LabVIEW program. During the measurements, a small ac signal of 20 mV is superimposed on a dc biasing voltage. The ac signal aids in the capacitance measurements. The measurements are done over a frequency range of 20 Hz to 1 MHz with a scan rate of 0.05 V/s.

### C. EFISHG background and setup

In nonlinear optics, the induced polarization is expressed as a power series in the electric field strength  $\vec{E}(t)$ :

$$\vec{P}(t) = \varepsilon_0 \left( \chi^{(1)} \vec{E}(t) + \chi^{(2)} \vec{E}(t)^2 + \chi^{(3)} \vec{E}(t)^3 + \dots + \chi^{(n)} \vec{E}(t)^n \right), \quad (1)$$

where  $\chi^{(2)}$ ,  $\chi^{(3)}$ ,  $\chi^{(n)}$  are the second-, third-, and in general,  $n$ th-order nonlinear optical susceptibility, which play a role in the strong-field regime. The nonlinear polarization further modulates the propagation of light in dielectrics, resulting in the generation of the outgoing light with a different frequency as in SHG and third-harmonic generation (THG) along with modulating the incident light field [24]. SHG results in doubling the frequency of the incident light and demands that the inversion symmetry of the system is broken. One mechanism of breaking the centrosymmetry of a molecule is by the application of an external electric field, which is central to the EFISHG mechanism. In general, EFISHG is a third-order process, described by a nonlinear optical polarization:

$$P_i^{2\omega} = \chi_{ijk}^{(3)}(-2\omega; \omega, \omega, 0) E_j^\omega E_k^\omega E_l^0. \quad (2)$$

In Eq. (2),  $E_l^0$  is the applied field and  $E_j^\omega E_k^\omega$  represent the laser field.  $\chi_{ijk}^{(3)}$  is the third-order nonlinear optical susceptibility. The application of a drain-source voltage in the

parallel direction in a FET (with respect to the incident laser field and with appropriate polarization condition) may be viewed as a symmetry-breaking phenomenon as the induced dipole moment couples with the applied electric field. This allows the observation of bulk coherent SHG and consequently, Eq. (2) may be written such that it resembles a second-order nonlinear effect [25]:

$$P_i^{2\omega} = \chi_{ijk}^{(2)}(-2\omega; \omega, \omega) (E^0) E_j^\omega E_k^\omega, \quad (3)$$

where  $\chi_{ijk}^{(2)}(-2\omega; \omega, \omega) (E^0) = \chi_{ijkl}^{(3)}(-2\omega; \omega, \omega, 0) E_l^0$ . The intensity of the SHG light is thus  $I^{2\omega} \propto |P(2\omega)|^2$ . Furthermore,

$$I^{2\omega}(x) \propto \left| \int_{-\infty}^{\infty} E(x') I^\omega(x-x') dx' \right|^2, \quad (4)$$

where  $\int_0^L E(x') dx' = V_{DS}$  and  $I^\omega$  is the intensity of the fundamental wavelength. The total electric field in the channel region is the sum of the Laplace field (due to the external source) and the Poisson field (the space-charge field due to injected charges). Equation (4) reduces to  $I^{2\omega}(x) \propto |E(x)|^2$  as the incident laser typically uniformly illuminates the entire channel region.

The experimental setup for EFISHG is shown in Fig. 1. The excitation wavelength is provided by a tunable (1120 nm–20  $\mu\text{m}$ ) optical parametric amplifier (TOPAS). The TOPAS is pumped by a regenerative amplifier (Spitfire Ace, Spectra Physics) with a repetition rate of 1 kHz, pulse duration of 100 fs, and seeded by an 80-MHz Ti-sapphire laser (MaiTai, Spectra Physics). A beam expander is placed before a long-working-distance microscopic objective to ensure that the entire channel region of the FET is illuminated. The EFISHG images are collected by an EMCCD camera (Photometrics Evolve 512). A band-pass filter (BG39) is used before the camera for removing the fundamental IR component and another band-pass filter at twice the frequency of the incident light is placed before the camera for allowing only the SHG light and rejecting other wavelengths. The setup is also equipped with a spectrometer and a CCD for spectroscopic measurements.

The FETs are used in three different configurations: one corresponding to the saturation condition with the application of drain-source ( $V_{DS}$ ) and gate-source ( $V_{GS}$ ) voltages, the second case is only the application of  $V_{GS}$ , ensuring injection of carriers, but  $V_{DS}$  is zero, and in the last case only  $V_{DS}$  is applied (without any injection of carriers). This last case results in a SHG signal, which is indicative of the Laplace field. The voltage pulse and the laser pulse are time delayed, as shown by the dotted blue box, by a pulse-delay generator (TOMBAC, AlphaNov).

For nonlinear optical imaging, it is crucial that the dispersion of the fs pulses are compensated. Since there is a significant group-velocity dispersion (GVD) associated

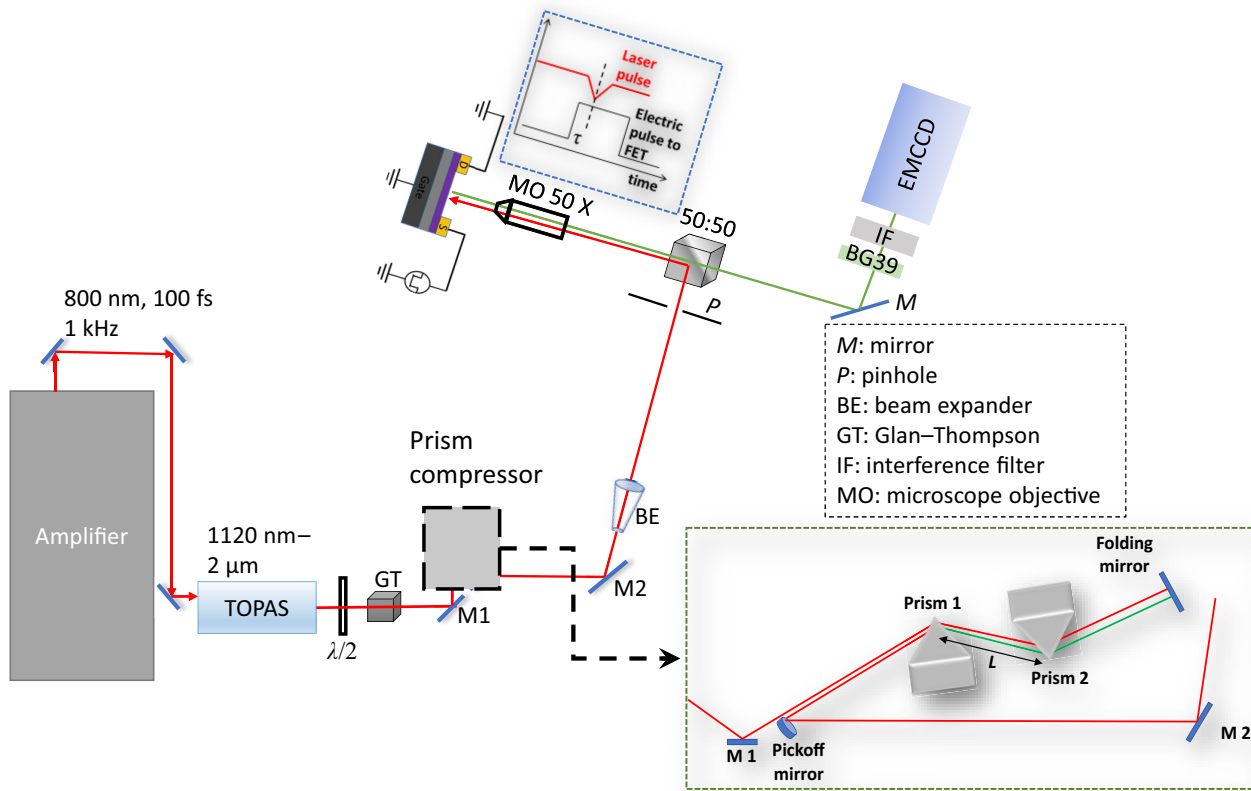


FIG. 1. Schematic of the EFISHG imaging setup. The blue dotted box illustrates the time delay between the laser pulse and the electrical signal applied to the transistor. The green dotted box shows the two-prism compressor assembly.

with fs pulses as they are transmitted through the cubic beam splitter and microscopic objective, there is temporal distortion [26,27]. A pair of prisms (green dotted box in Fig. 1), where the separation between them may be adjusted, is used to compensate the GVD for each of the incident wavelengths required for EFISHG imaging. There are two purposes of using the prism pair; to compensate the fs distortion due to the GVD of optics and to spectroscopically clean up the laser wavelength from the TOPAS. Details of the prism compressor assembly setup are included within the Supplemental Material [28].

### III. RESULTS AND DISCUSSIONS

#### A. FETs in the operational regime

Various BGTC geometry FETs are fabricated using different dielectric layers. This is the ideal geometry for EFISHG since the organic semiconducting layer can be accessed directly by the incident light, without exciting additional layers. However, EFISHG can also be measured from top-gate, bottom-contact (TGBC) geometries as shown in our recent work for *n*-type organic FETs [29]. We use pentacene and a solution processable donor-acceptor copolymer, DPP-DTT, as semiconducting layers.

DPP copolymers have high air stability, are robust, and demonstrate high carrier mobilities in FET architectures [30–32]. Prior to measuring the EFISHG signal from the FETs, basic electrical characteristics are measured to determine the transistor performance. The output characteristics are determined by sweeping  $V_{DS}$  and measuring the drain current ( $I_D$ ) for different values of  $V_{GS}$ . By noting the saturation region, the transfer characteristics display  $I_D$  as a function of  $V_{GS}$  at a fixed  $V_{DS}$  (in the saturation region). Knowing the channel length ( $L$ ) and width ( $W$ ), the saturation region carrier mobility ( $\mu$ ) is given by  $\mu_{\text{sat}} = (2L/WC_i)(\partial\sqrt{I_D}/\partial V_{GS})^2$ , where  $C_i$  is the capacitance of the dielectric layer. Typically, the mobility is also extracted in the linear region and is given by  $\mu_{\text{lin}} = (L/WV_{DS}C_i)\partial I_D/\partial V_{GS}$ . In an ideal device, where contact resistance is not significant,  $\mu_{\text{sat}} = \mu_{\text{lin}}$ . Other parameters of interest are the threshold voltage ( $V_{\text{th}}$ ), *on:off* ratio, and the subthreshold swing ( $SS$ ), which is given by  $\{[\partial\log(I_D)]/\partial V_{GS}\}^{-1}$ .

The EFISHG experiments are conducted by applying pulsed  $V_{DS} = V_{GS}$  (saturation region condition). Since the EFISHG intensity depends on  $\chi^{(3)}$ , it is a weak phenomenon; hence, the choice of the incident wavelength is critical and should be selected such that it maximizes  $\chi^{(3)}$ .

The SHG response of a material depends on the resonance enhancement of the dipole interaction or it is due to a quadrupole process. The latter allows a transition between the ground state and a forbidden excited state. It is this quadrupole process that plays a role in pentacene, as shown in Ref. [33], where the SHG signal at 560-nm pentacene is seen from all interfaces. Hence for EFISHG experiments, where the SHG peak is observed under the application of an electric field, the fundamental wavelength of 1120 nm is a good choice.

Alternately, measuring the THG from a film gives an estimate of the enhancement of  $\chi^{(3)}$  with the incident wavelength, and thus the resonance condition. We demonstrate this for the DPP-DTT system in Fig. 2. The third-harmonic (TH) generation is monitored from a thin film of DPP-DTT as a function of the incident wavelength. Maximum TH intensity is observed when the incident wavelength is at 1500 nm. A power dependence of the TH spectrum at this wavelength is shown in the inset. Unlike pentacene, where there is a symmetry breaking due to an interface effect, SHG is not observed from a DPP-DTT film deposited on glass. Hence the THG signal is a guidance to

the resonance condition. This implies that under EFISHG conditions, the 1500-nm wavelength will give the maximum signal. The SHG at 750 nm, observed under EFISHG conditions, is just below the absorption maxima of the sample [28,34].

### 1. Pentacene FETs with different dielectrics

TR EFISHG images are captured from three different BGTC pentacene FETs with gate dielectrics as PMMA, SiO<sub>2</sub>, and cPVP. In all cases, the FETs are *p* type. For SiO<sub>2</sub> and PMMA, the saturation region condition ( $V_{DS} = V_{GS} = -40$  V) is used, whereas for cPVP, linear region condition of  $V_{DS} = V_{GS} = -10$  V is used. Since the EFISHG intensity is proportional to the applied voltage, there is almost no signature observed below 10 V from pentacene FETs. Figure 3(a) shows the TR EFISHG images from a pentacene/PMMA FET for different delay times with a fundamental wavelength of 1120 nm, which is *s* polarized. As the carriers are injected, these images display their transit from the source to the drain terminal. When the delay time is 0, there is hardly any SHG signal but as time progresses, a clear movement of the induced polarization, representing carrier motion (denoted by the red arrow), is observed. Since the injected carriers are holes, the direction of movement of the induced polarization is from the source to the drain electrode, which is reversed in *n*-type FETs [29].

The plot profiles of the images are shown in Fig. 3(c). Along with the movement of the polarization wave front from the source to the drain terminal, a decrease in EFISHG intensity is observed beyond 1.5  $\mu$ s. Since a space-charge field is setup with the injection of carriers in the FET channel, it negates the original Laplace field and reduces the overall EFISHG intensity. The transit time of carriers is typically given by  $\tau = L^2/\mu V$ , which is based on the drift model of a two-terminal device. Here,  $V$  is the applied voltage and  $L$  is the distance traversed by the carriers. It was shown by Weis *et al.* that for a three-terminal device, where an additional charge accumulation between the semiconducting and the insulating layer is formed, the Maxwell-Wagner model is more appropriate to deduce the transit time of the carriers across the FET channel [22]. As long as  $|V_{GS} - V_{th}| \gg |V_{DS}|/2$ , the transit time of the carriers from the source to drain across the semiconductor-insulator interface is given by [22]

$$\tau = \frac{L^2}{\mu(V_{GS} - V_{th} - V_{DS}/2)}. \quad (5)$$

A Gaussian peak is assumed for the position of the polarization wave front from where  $L$  is deduced. The error bars shown for the individual  $L^2$  values are determined from the full width at half maximum of the Gaussian profiles (of the induced polarization wave). A broadening of the

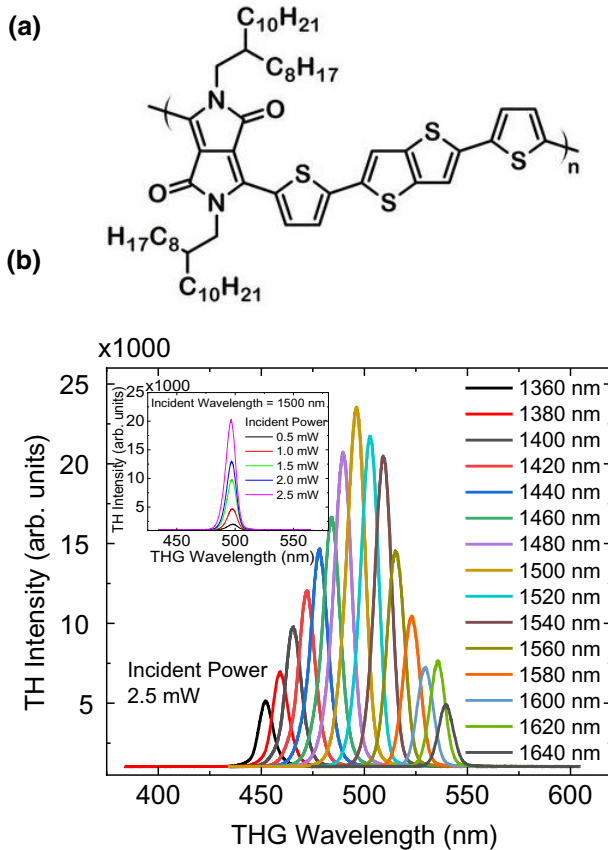


FIG. 2. Third-harmonic generation from DPP-DTT. (a) Chemical structure of DPP-DTT. (b) The TH intensity from a film of DPP-DTT as a function of the incident wavelength. The inset shows the power dependence of the THG profile for the fundamental wavelength of 1500 nm.

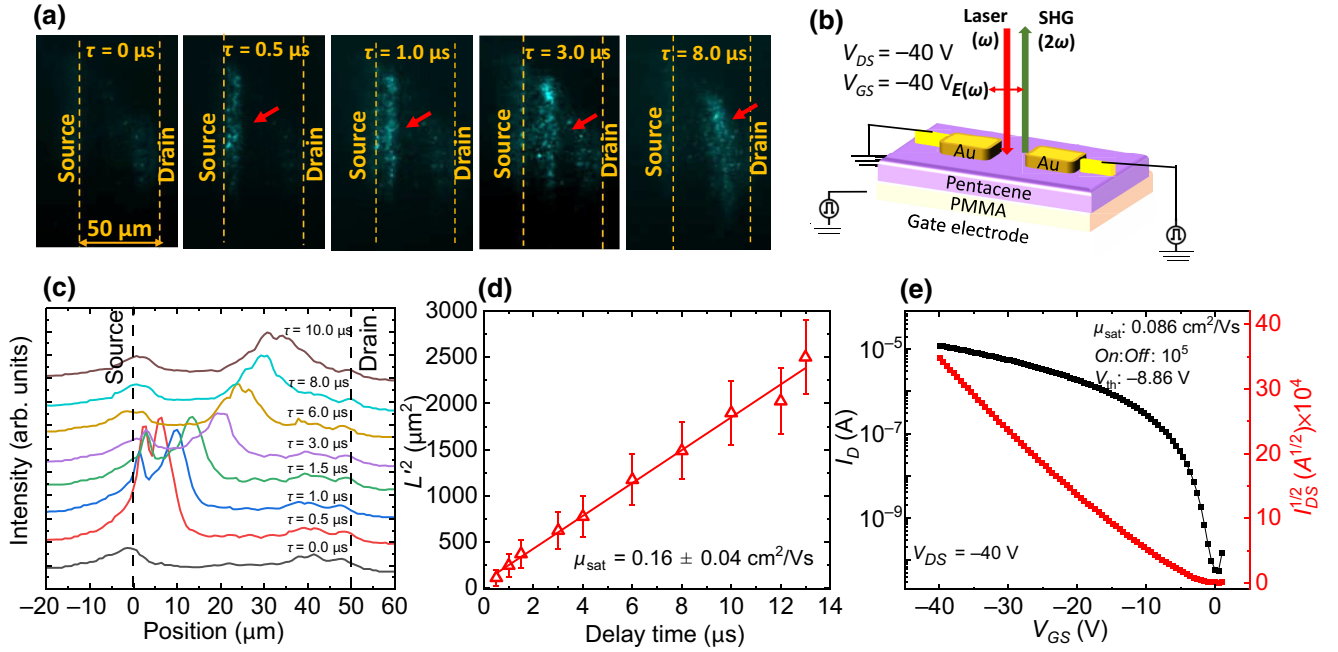


FIG. 3. EFISHG from pentacene/PMMA FETs. (a) TR EFISHG images from a pentacene/PMMA FET biased under saturation conditions for a few selected time delays. The red arrow depicts the position of the wave front. (b) Schematic of the FET. *s*-polarized laser light is incident on the sample. (c) Plot profiles determined from EFISHG images for various delay times. (d) The position of the induced polarization wave front ( $L^2$ ) as a function of the delay time. (e) The transfer characteristics of the same FET used for EFISHG measurements.

Gaussian peaks occurs with increasing delay time due to the setting up of a space-charge field in the channel upon injection of carriers. The error bar associated with the carrier mobility is from a linear fit of the  $L^2$  versus delay time plots by explicitly considering the  $y$  error of the data. We plot  $L^2$  versus  $\tau$  in Fig. 3(d) and by using Eq. (5), obtain the carrier mobility as  $0.16 \pm 0.04$   $\text{cm}^2/\text{Vs}$ . This is almost twice the value obtained from the transfer characteristics [Fig. 3(e)]. The carrier mobilities are tabulated in Table I. To obtain a deeper insight into the differences between the carrier mobilities obtained by electrical measurements versus EFISHG measurements, we fabricate pentacene FETs with different dielectrics, estimated

TABLE I. The carrier mobilities extracted from current-voltage characteristics, TR EFISHG measurements, and the contact resistance of pentacene and DPP-DTT FETs. The terms in brackets in the second column denote the dielectric permittivity. All FET mobilities are obtained in the saturation region except for pentacene and cPVP, which is in the linear region.

Semiconductor	Dielectric	$\mu_{\text{electrical}}$ ( $\text{cm}^2/\text{Vs}$ )	$\mu_{\text{EFISHG}}$ ( $\text{cm}^2/\text{Vs}$ )	$R_C W$ ( $\text{k}\Omega$ $\text{cm}$ )
Pentacene	SiO <sub>2</sub> (4)	0.06	$0.29 \pm 0.07$	79.7
	PMMA (3.5)	0.09	$0.16 \pm 0.04$	73.8
	cPVP (4.5)	0.06	$0.22 \pm 0.06$	70.4
DPP-DTT	PMMA (3.5)	0.03	$0.66 \pm 0.09$	263.7

contact resistances, and obtain the interface trap density in a few devices from capacitance and conductance versus voltage measurements.

The results from SiO<sub>2</sub>/pentacene FETs are shown within the Supplemental Material [28]. Here again, a clear movement of the induced polarization wave front is observed from source to drain as the delay time is changed. EFISHG measurements yield  $\mu = 0.29 \pm 0.07$   $\text{cm}^2/\text{Vs}$  whereas transfer characteristics yield  $0.06$   $\text{cm}^2/\text{Vs}$  (for  $V_{DS} = -40$  V and sweeping  $V_{GS}$  to  $-40$  V).

Pentacene FETs with cPVP as the dielectric layer do not completely saturate at voltages less than 10 V. We use this as a test case for comparing carrier mobilities obtained in the linear region. In this case, the voltages are set to  $V_{DS} = V_{GS} = -10$  V. Figure 4(a) shows snapshots of TR EFISHG images for a few delay times. The red arrows denote the movement of the wave front. We note that the source terminal is on the right-hand side in this case. The plot profile [Fig. 4(c)] clearly shows the movement of the carriers from the source to the drain. Beyond 35  $\mu\text{s}$ , no motion of the polarization wave front is observed, indicating that the transit time of the carriers is over. We obtain a carrier mobility of  $0.22 \pm 0.06$   $\text{cm}^2/\text{Vs}$ ; in comparison, the average carrier mobility obtained from the linear region of the transfer characteristics is  $0.06$   $\text{cm}^2/\text{Vs}$ .

Although similar integration times are used for obtaining EFISHG images from all FETs, the background can

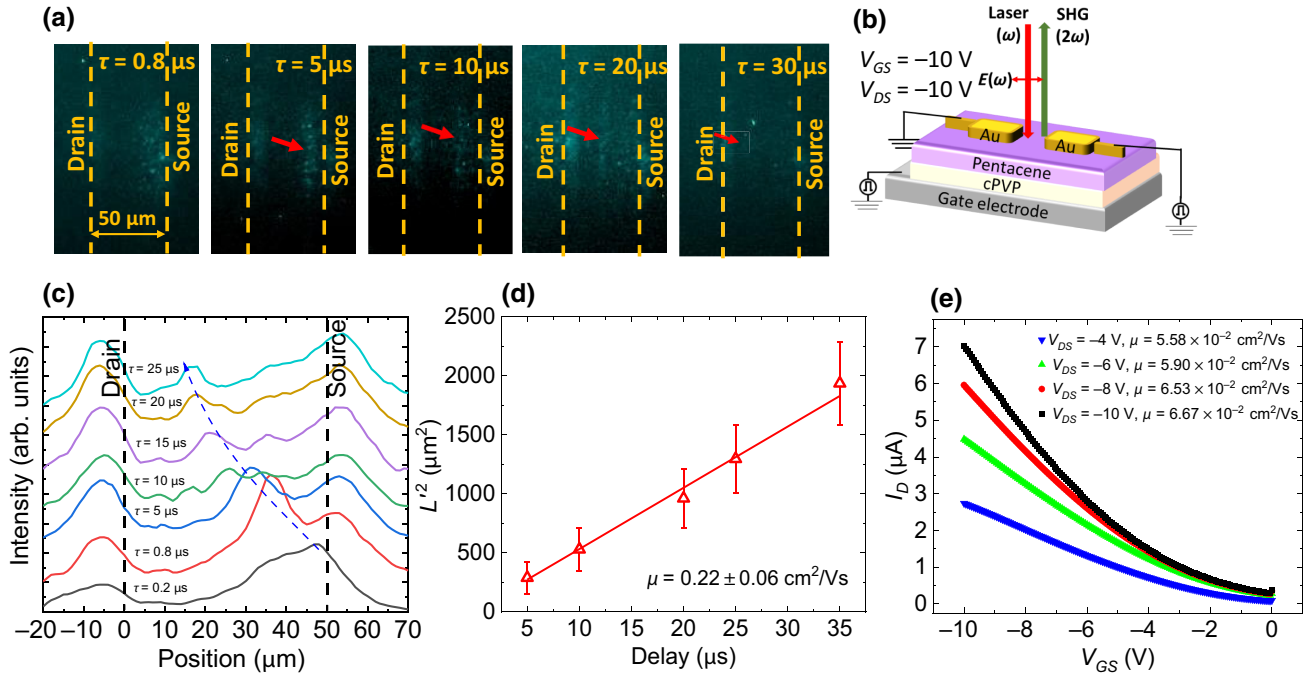


FIG. 4. EFISHG from pentacene/cPVP FETs. (a) TR EFISHG images from a pentacene/cPVP FET biased in the linear region ( $V_{DS} = V_{GS} = -10 \text{ V}$ ) for a few selected time delays. The red arrow shows the position of the wave front. (b) Schematic of the FET and experimental conditions. (c) Plot profiles determined from EFISHG images for various delay times. The blue dotted line is a guide to the eye, showing the motion of the carriers from source to drain. (d) The position of the induced polarization wave front ( $L^2$ ) as a function of the delay time. (e) The transfer characteristics in the linear region of the same FET used for EFISHG measurements.

differ depending on the dielectric used. The OH groups in cPVP make it highly polarizable (as seen in capacitance-voltage measurements, discussed in the next section), which may contribute to a higher SHG background in all images. However, since TR EFISHG tracks the motion of carriers as a function of the delay time, one can still capture the movement of the wave front from any background signal.

The three dielectrics used in pentacene FETs have slight variations in the dielectric constant ( $\kappa$ ). Due to a dynamic coupling of the charge carriers with the electronic polarization at the semiconductor-dielectric interface via the formation of surface polarons, carrier mobilities extracted from current-voltage characteristics are suppressed with increase in  $\kappa$  of the dielectric layer [35]. The effect is pronounced when ferroelectric dielectrics are used, for example [7,36,37]. We see a hint of this in the pentacene FETs; PMMA, which has the lowest value of  $\kappa$ , shows the highest carrier mobility of  $0.09 \text{ cm}^2/\text{Vs}$  from electrical measurements (Table I). This trend is, however, not observed from carrier mobilities extracted from TR EFISHG measurements as the carrier motion arises due to the electric field of the carrier sheet. Another difference one observes is that  $\mu_{\text{EFISHG}}$  is 2–5 times higher than  $\mu_{\text{electrical}}$ . This is expected since the contact resistance does not play a role in TR EFISHG. We discuss the issue of contact

resistance in more detail after presenting the results of the polymer-based FET.

## 2. DPP-DTT FET with PMMA as the dielectric

To further understand the role of the semiconductor-dielectric interface in TR EFISHG, we use a solution-processable polymer, DPP-DTT, as the active layer along with PMMA as the dielectric layer. In this geometry, the FET is predominantly  $-p$  type. It should be kept in mind that DPP-DTT is ambipolar; with a top-gate geometry,  $n$ -type behavior is often observed [34]. For maximizing the EFISHG signal, the fundamental wavelength is selected at  $1500 \text{ nm}$ . Figure 5(a) shows the EFISHG images from a DPP-DTT FET for four different delay times. The background is stronger than pentacene FETs, which may be related to a higher  $\chi^{(3)}$  value. The progression of the carrier wave front can be easily seen despite the high background from source to drain (right to left). The plot profiles [Fig. 5(c)] show that by  $4 \mu\text{s}$ , the transit of the carriers from the source to the drain terminal is complete. We also change the polarity of the applied voltage; TR EFISHG images show no movement of carriers signaling that the BGTC geometry with PMMA as the dielectric layer predominantly yields  $p$ -type behavior. By locating the position of the carrier wave front in the EFISHG

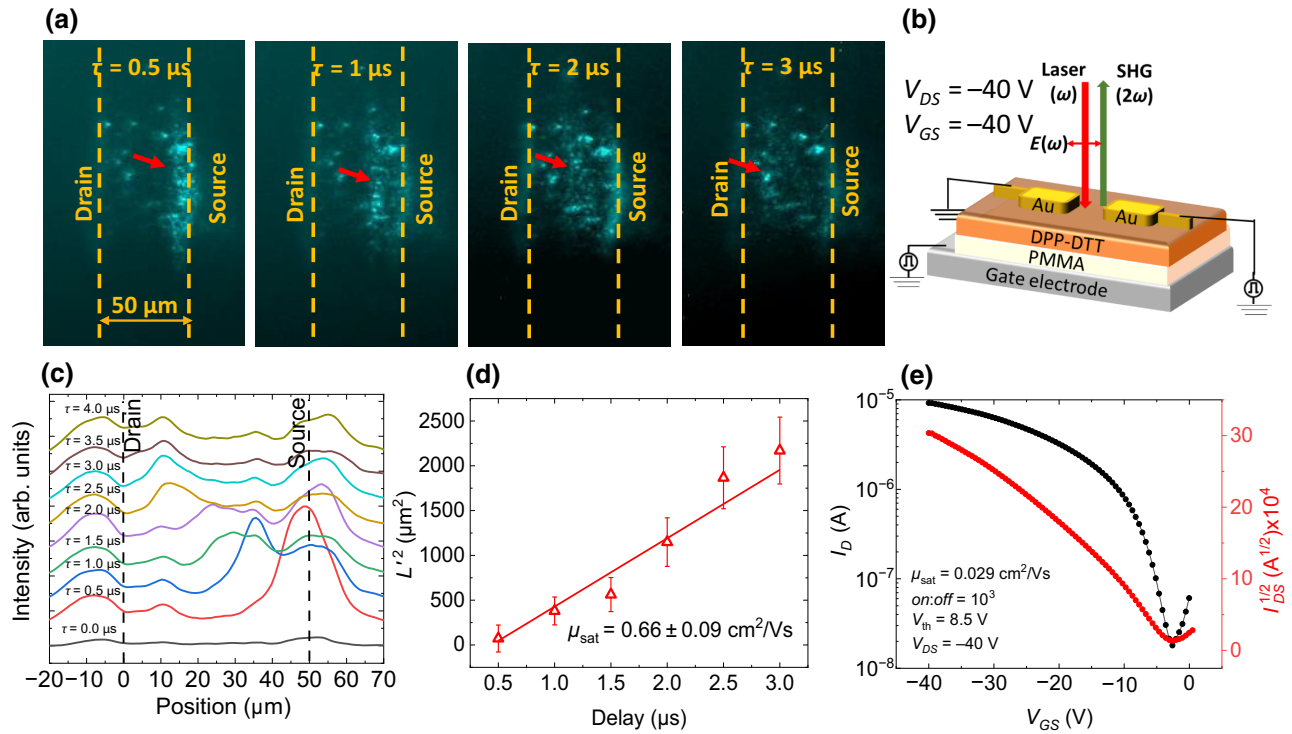


FIG. 5. EFISHG from DPP-DTT/PMMA FETs. (a) TR EFISHG images from a DPP-DTT/PMMA FET biased in the saturation region ( $V_{DS} = V_{GS} = -40 \text{ V}$ ) for a few selected time delays. The red arrows depict the position of the carrier wave front. (b) Schematic of the FET and the experimental conditions. (c) Plot profiles determined from EFISHG images for various delay times. (d) The position of the induced polarization wave front ( $L^2$ ) as a function of the delay time. (e) The transfer characteristics of the same FET.

images, the  $p$ -type carrier mobility is obtained as  $0.66 \pm 0.09 \text{ cm}^2/\text{Vs}$ , which is more than 22 times obtained from the transfer characteristics [Fig. 5(e)].

The difference between  $\mu_{\text{EFISHG}}$  and  $\mu_{\text{electrical}}$  mainly stems from the contact resistance, which arises from non-Ohmic contacts at the source and drain, resulting in a voltage drop near the two electrodes [38]. Additionally, trap states play a role as well. For each FET, the contact resistance (normalized with  $W$ ) is determined using the transmission-line method [39], where the linear region of the output curve gives  $RW = R_C W + L / (\mu_{\text{eff}} C_i (V_{GS} - V_{\text{th}}))$ ; here,  $R$  is the total resistance,  $R_C$  is the contact resistance, and  $\mu_{\text{eff}}$  is the carrier mobility free of the contact resistance. Since  $R_C$  for the DPP-DTT FET is higher than the pentacene FETs, one can rationalize the large difference between the carrier mobilities obtained from TR EFISHG and electrical methods. These results, therefore, suggest that by judicious reduction in the contact resistance, the carrier mobility measured from the transfer characteristics in DPP-DTT FET may be enhanced by at least 20 times. Additionally, the trapped charge density plays a role in the electrical measurements, which is less of an issue in TR EFISHG since the induced polarization is what is tracked (see Supplemental Material for more details [28]). Alternative intrinsic mobility determination techniques such as charge extraction (of injected

carriers) by linearly increasing voltage measurements provide useful insights into semiconductor thin-film devices and estimate accurate carrier mobilities at non-Ohmic contacts [40]. Such measurements from organic FETs in the future will be beneficial for comparing carrier mobilities obtained from TR EFISHG images.

In addition to obtaining insights into charge-carrier mobilities intrinsic to the semiconducting film, the TR EFISHG technique gives valuable information on interface charging, which is directly related to the formation of the accumulation layer at the semiconductor-dielectric interface. This is discussed in the next section.

## B. FETs in the nonoperational regime

### 1. Formation of the accumulation layer

There is a wealth of information one can obtain from EFISHG images while the FET is in a nonoperational regime. We first discuss the situation where only  $V_{GS}$  is applied and  $V_{DS} = 0$ . This condition will result in the injection of charges without any drift current in the source-drain direction. Since both source and drain electrodes are at the same potential, charges are injected from both electrodes, and owing to the gate being more negative ( $p$ -type FETs), the charges (holes) drift towards the gate. In TR EFISHG images, the charges are seen to migrate to the center of

the channel, reflecting an interface charging effect due to the electric field across the interface. The Maxwell-Wagner model is still valid, where the transit time is related to the mobility of the carrier sheet [Eq. (5)] with  $V_{DS} = 0$ . In order to look at the role of the semiconductor-dielectric interface in this mode, we mainly compare the pentacene/PMMA and DPP-DTT/PMMA FETs (other FETs are shown within Supplemental Material [28]). The results from nonlinear optical images are further compared with the interface trap density and carrier concentration measured from capacitance and conductance versus voltage characteristics.

When  $V_{DS} = 0$ , classifying drain and source electrodes is not really meaningful. However, source and drain electrodes in these measurements refer to the same when the FETs are under operation. Figure 6(a) shows selected TR EFISHG images of the movement of the charge-carrier wave front as a function of the delay time with  $V_{DS} = 0$  and  $V_{GS} = -40$  V from pentacene/PMMA FET (the same device that is measured in Fig. 3). The slightly higher SHG intensity near the right electrode (drain) is reflective of an asymmetric electric field of the laser field; it does not necessarily suggest a higher charge injection from the drain electrode. The plot profile in Fig. 6(c) clearly shows the carrier sheet to move inwards from both electrodes. By

measuring the edge of the wave front as a function of position from both electrodes [Figs. 6(d) and 6(e)] and using Eq. (5), the mobility is estimated as  $0.044 \pm 0.01$  cm<sup>2</sup>/Vs from source and  $0.032 \pm 0.01$  cm<sup>2</sup>/Vs from drain. As such, the Maxwell-Wagner theory predicts the mobility of carriers in this configuration to be 1/2 of the mobility of the carriers under normal operating conditions.

Comparing pentacene/PMMA FET with DPP-DTT/PMMA FET, we see several differences. Shown in Fig. 7(a) are the TR EFISHG images from the DPP-PMMA FET for selected delay times under the condition  $V_{DS} = 0$  and  $V_{GS} = -40$  V. Here, the SHG intensity from both electrodes are similar and again a clear movement of the charges towards the center of the channel is observed from both electrodes as a function of the transit time. The mobility of the carrier wave front from the source and drain electrodes is almost similar (average  $0.26$  cm<sup>2</sup>/Vs), and this value is approximately 1/2 the carrier mobility under normal operation.

Before discussing the differences between the pentacene/PMMA and DPP-DTT and pentacene devices, we note that interface charging effects are also observed in pentacene/SiO<sub>2</sub> and pentacene/cPVP FETs with the application of only  $V_{GS}$  (see Supplemental Material [28]). In pentacene/cPVP, the two wave fronts seem to merge,

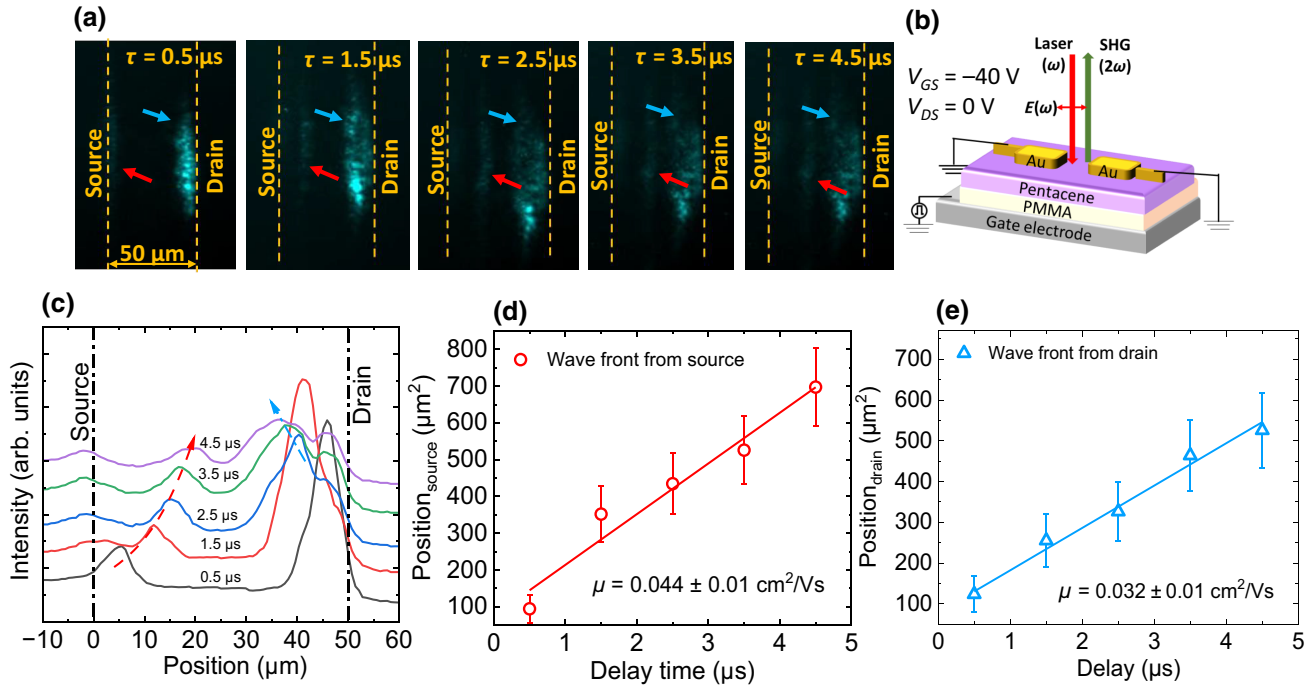


FIG. 6. Interface charging in pentacene/PMMA FETs. (a) TR EFISHG images from pentacene/PMMA FET for a few selected delay times under biasing conditions of  $V_{DS} = 0$  and  $V_{GS} = -40$  V. The red and the blue arrows indicate the carrier wave front from the source and drain electrodes. (b) Schematic of the FET with the specific biasing condition. (c) Plot profiles determined from the EFISHG images for varying delay times. The red and blue dotted lines show the movement of the charges towards the center of the channel. (d) The position of the polarization wave front from the left electrode (source) as a function of the delay time. (e) The position of the induced polarization wave front from the right electrode (drain) as a function of the delay time.

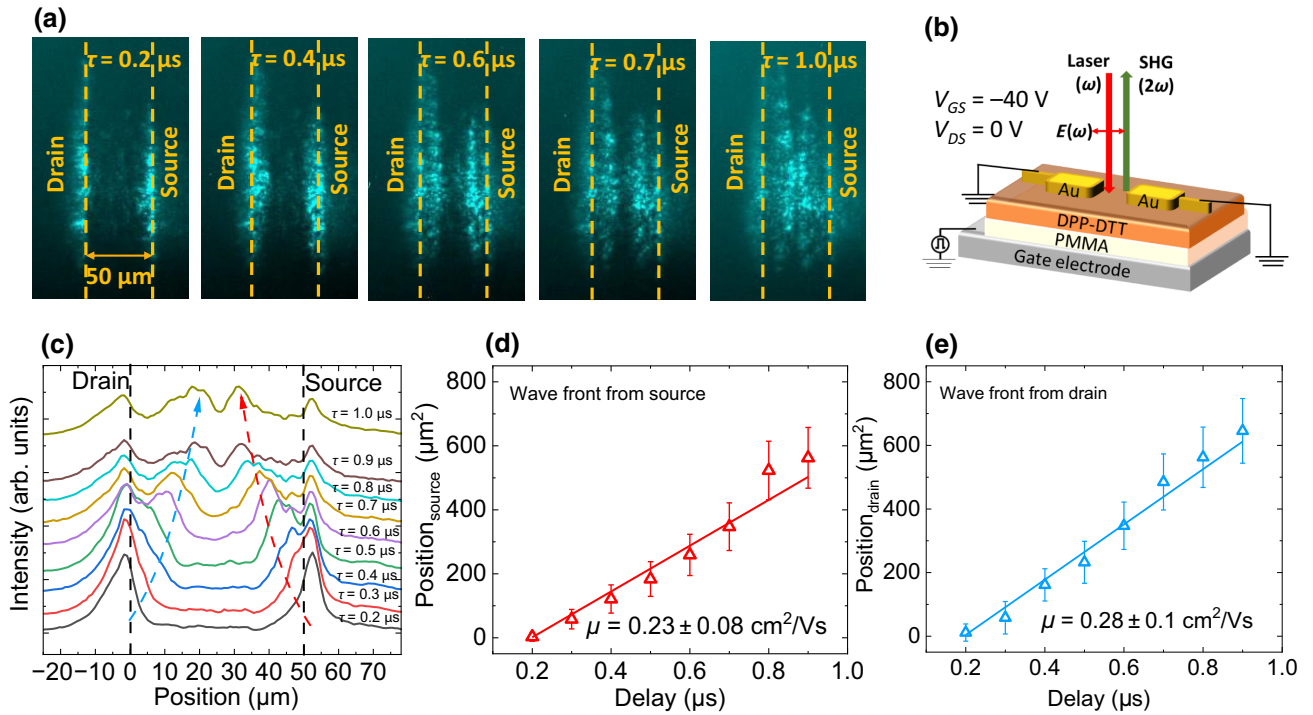


FIG. 7. Interface charging in DPP-DTT/PMMA FETs. (a) TR EFISHG images from DPP-DTT/PMMA FET for a few selected delay times under biasing conditions of  $V_{DS} = 0$  and  $V_{GS} = -40 \text{ V}$ . (b) Schematic of the FET with the specific biasing condition. (c) Plot profiles determined from the EFISHG images for varying delay times. The red and blue dotted lines show the movement of the charges towards the center of the channel. (d) The position of the polarization wave front from the left electrode (source) as a function of the delay time. (e) The position of the induced polarization wave front from the right electrode (drain) as a function of the delay time.

thus making it difficult to obtain the carrier mobilities. Capacitance-voltage characteristics from a two-terminal pentacene/cPVP *M-I-S* structure shows a large hysteresis, which most likely arises due to the O-H groups in cPVP. We believe that the inherent polarization of the dielectric medium is the reason why the interface charging effect is not clearly observed in cPVP-based FETs.

During the operation of the FET, the propagation of charges in the channel is not just due to  $V_{DS}$  but there is an influence of the interface charging as well. Upon injection, the charges form an accumulation layer, and the redistribution of charges depend on the speed with which they reach the interface. Typically, scanning probe microscopy such as Kelvin probe has been used for monitoring the channel carrier density and formation of the accumulation layer [41]. TR EFISHG provides an alternative visual tool for observing the formation of the accumulation layer in organic FETs. Our results highlight that the same semiconductor may show very different migration of carriers towards the interface if the dielectric layer is modified. As such, changing the semiconductor but having the same dielectric layer will result in different carrier mobilities due to the nature of transport inherent to the active layer, but that does not explain the discrepancy observed in the mobilities of the carrier wave front when both  $V_{DS}$  and  $V_{GS}$

are applied versus when only  $V_{GS}$  is present; the Maxwell-Wagner theory predicts that with the application of only  $V_{GS}$ , the transit time of the carriers should be twice or the mobility should be 1/2 compared to when both  $V_{DS}$  and  $V_{GS}$  are present.

## 2. Metal-insulator-semiconductor diodes

In order to understand the interface charging results from pentacene/PMMA and DPP-DTT/PMMA FETs, we look more closely at the interface trap densities deduced from *C-V* and *G-V* measurements. The interface traps change their occupancy over a small energy range about the Fermi level by interacting with the semiconductor bands via the emission and capture of carriers. Typically, upon the application of a small ac signal to a *M-I-S* diode, the band edges move toward or away from the Fermi level. The conductance technique enables the extraction of the interface trap density ( $D_{it}$ ) from the loss, which changes the occupancy of the interface trap states when a dc gate bias is varied [42]. The  $D_{it}$  values account for a lag time as the Fermi level crosses an occupied trap state and the time for the trap to empty. The signature of a conductance peak is due to the ac loss as a result of capture and emission of carriers by these interface states. Depending on the assumed

energy distribution of the interface traps, either a single time constant or a continuum of states model of the conductance method is used to estimate  $D_{it}$  [43]. Most organic semiconductors are appropriately modeled by the continuum of states model, where the interface traps are assumed to have energy levels that are closely spaced across the band gap and thus, treated as a continuum of states [44,45]. In this model, the equivalent parallel conductance ( $G_p$ ) extracted at different biases from the measured capacitance and conductance is given by [42]

$$\frac{G_p}{\omega} = \frac{qD_{it} \ln(1 + \omega^2 \tau'^2)}{2\omega \tau'}, \quad (6)$$

where  $\tau'$  is the interface time constant and  $G_p/\omega$  has a maximum at  $\omega \tau' = 1.98$ . Although the general mechanism of transport in organic semiconductors is different from Si and inorganic semiconductors, the concept of a mobility edge, which plays the same role as band edges in a crystal, is often used in disordered systems to discuss transport [37]. Equation (6) is based on a continuum of states model for a Si-based MOS device, which mimics the distribution of states in most organic semiconductors; hence conventional  $G$ - $V$  and  $C$ - $V$  analysis is applicable to organic  $M$ - $I$ - $S$  devices [43].

The  $C$ - $V$  characteristics from the  $M$ - $I$ - $S$  diodes are provided within the Supplemental Material [28]. Unlike pentacene/PMMA, the DPP-DTT/PMMA  $M$ - $I$ - $S$  diode shows a slight hysteresis (Fig. S11 within the Supplemental Material) [28]. The accumulation capacitances in both are approximately the same, suggesting that the thickness of the PMMA layer is similar for both devices. Using a positive-to-negative sweep, we determine the flat-band voltage (FB) as  $-1.6$  V for pentacene  $M$ - $I$ - $S$  and  $-13.7$  V for the DPP-DTT  $M$ - $I$ - $S$ . Figures 8(a) and 8(c) display the loss ( $G_{\text{measured}}/\omega$ ) as a function of the gate bias for both pentacene/PMMA and DPP-DTT/PMMA  $M$ - $I$ - $S$  diodes. A clear loss peak is absent in either of the devices, suggesting that the capture and emission of carriers is dominated by the bulk trap levels with a slight contribution from interface states. From the  $C$ - $V$  plots in the depletion region, one can obtain the doping density (localized charge density),  $N_A$ , using the Schottky-Mott relationship:  $\partial(1/C^2)/\partial V_G = 2/q\epsilon_0\epsilon_{\text{semi}}N_A$ ;  $C$  is the capacitance density in the depletion region,  $\epsilon_0$  is the permittivity of vacuum, and  $\epsilon_{\text{semi}}$  is the relative permittivity of the semiconductor.  $1/C^2$  versus gate voltage is plotted in the inset of Figs. 8(b) and 8(d). Using  $\epsilon_{\text{semi}} = 3.6$  for pentacene [46] and approximating the same value for DPP-DTT, we obtain  $N_A$  to be  $2 \times 10^{16}$   $\text{cm}^{-3}$  for pentacene and an order of magnitude higher,  $2 \times 10^{17}$   $\text{cm}^{-3}$ , for DPP-DTT, similar to other DPP-based  $M$ - $I$ - $S$  structures [47].

The  $D_{it}$  values are obtained by using Eq. (6) and are plotted as a function of the gate bias in Figs. 8(b) and 8(d).

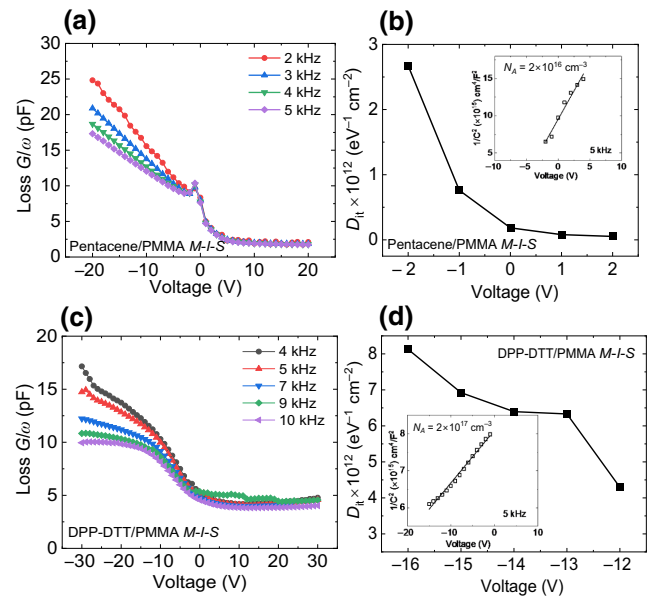


FIG. 8. Interface trap densities for pentacene/PMMA and DPP-DTT  $M$ - $I$ - $S$  devices. (a),(c) Loss (conductance and angular frequency) versus gate bias at various frequencies for pentacene and DPP-DTT  $M$ - $I$ - $S$  diodes, respectively. (b),(d) Interface trap density ( $D_{it}$ ) estimated from the depletion region in pentacene and DPP-DTT  $M$ - $I$ - $S$  diodes, respectively. The inset plots  $1/C^2$  versus voltage.

Since the FB is quite stretched in DPP-DTT, the depletion region occurs at a higher gate bias. The  $D_{it}$  value near the Fermi level is almost 3 times higher for the DPP-DTT/PMMA device ( $8 \times 10^{12}$   $\text{eV}^{-1} \text{cm}^{-2}$ ) compared with the pentacene/PMMA device ( $2.6 \times 10^{12}$   $\text{eV}^{-1} \text{cm}^{-2}$ ). The higher interface trap density may aid the interface-charging phenomenon observed in the DPP-DTT/PMMA FET. Additionally, an order of magnitude higher value of  $N_A$  in DPP-DTT/PMMA compared with pentacene/PMMA facilitates the charge distribution and formation of the accumulation layer more easily. We clearly see this in the TR EFISHG images under interface-charging conditions (Fig. 7). Not only is the mobility of the carrier sheet higher in the DPP-DTT FET compared with the pentacene FET, the left and the right wave fronts have almost the same transit times and exactly twice the value when the FET is operational (under the presence of both  $V_{DS}$  and  $V_{GS}$ ), following the Maxwell-Wagner model quite well.

### 3. Application of only $V_{DS}$

Application of only  $V_{DS}$  (with  $V_{GS} = 0$ ) will not inject any charges in the FET. However, the transverse field breaks the symmetry due to which SHG is allowed. Since there are no injected charges, there should be no motion of any carrier wave front in TR EFISHG with change in delay time. We demonstrate this for the pentacene/PMMA

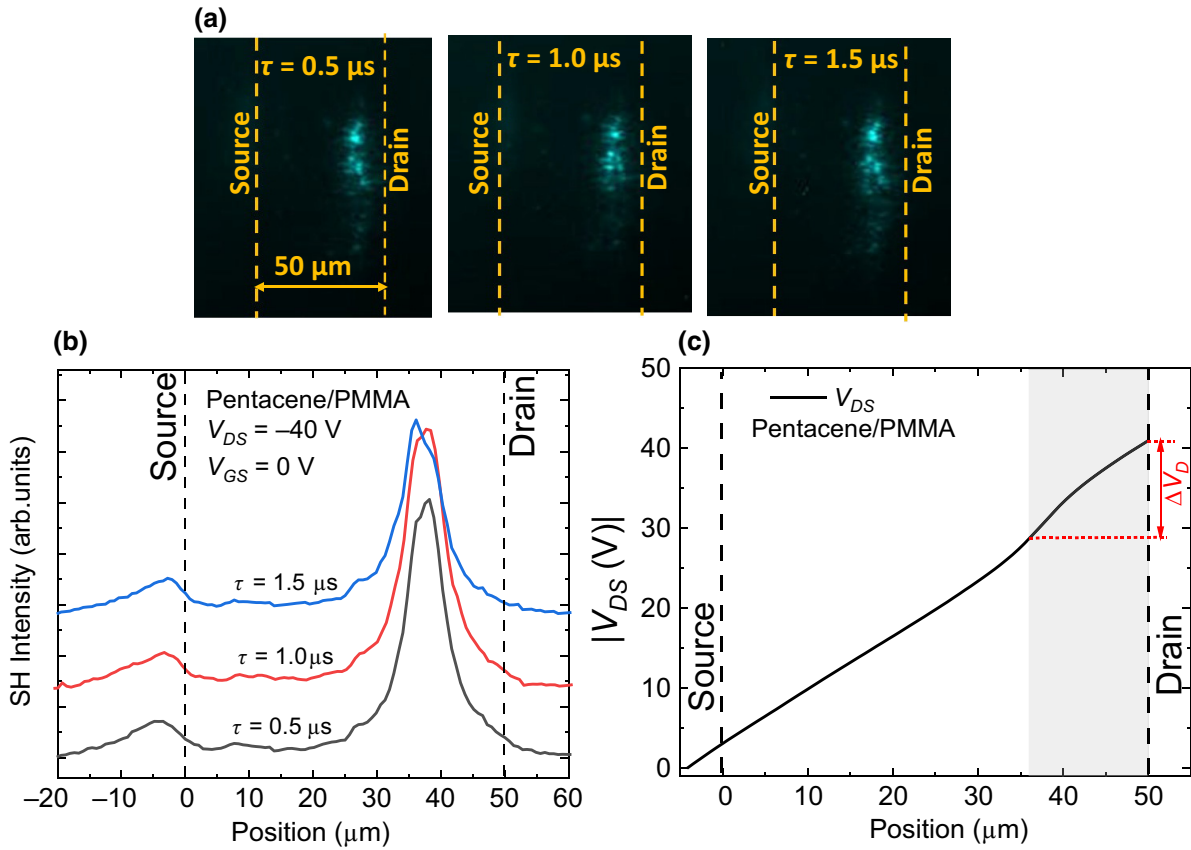


FIG. 9. Voltage mapping in pentacene/PMMA FET. (a) TR EFISHG images at three different delay times from pentacene/PMMA FET under the condition of  $V_{DS} = -40$  V and  $V_{GS} = 0$  V. (b) Plot profiles corresponding to the EFISHG images. (c) Voltage distribution in the channel region obtained from the EFISHG intensity.  $\Delta V_D$  corresponds to the voltage drop near the drain.

FET in Fig. 9. The TR EFISHG images and their plot profiles are shown in Figs. 9(a) and 9(b), respectively with  $|V_{DS}| = 40$  V for three different delay times. A maximum SHG is observed near the drain electrode, and as expected there is no motion of any charges with time since no charges are injected in this configuration. These observations further highlight that the incident light does not result in any photogenerated carriers, as that would have resulted in a propagation of the SHG signal in the channel region with increase in delay time.

From the EFISHG signal, one can estimate the electric field or the voltage inside the channel and any voltage drop near the electrodes. Such an analysis helps in visualizing the contact resistance in FETs. Using Eq. (4), we first estimate the electric field ( $\sqrt{I^{2\omega}(x)} \propto |E(x)|$ ) and upon integrating that value, a quantity proportional to the voltage is obtained. The absolute value of the voltage is plotted along the channel length in Fig. 9(c). An additional voltage drop ( $\Delta V_D$ ) near the drain electrode is observed, signaling the formation of an interface layer (depicted by the light gray region) near the electrode. Ideally, the voltage-drop near the source and drain electrodes should be negligible; however, the contact resistance in organic FETs can

be significant, resulting in a voltage drop near the contacts [38,48]. Although not as accurate as Kelvin-probe microscopy [41,49], EFISHG images give qualitative features into the electric field distribution within the channel region. In two-terminal organic bulk-heterojunction-type devices, such images have revealed the spatial distribution of the electric field; by monitoring the depletion region close to the electrode, Morris and co-workers could discern the stability of their devices [50].

#### IV. CONCLUSIONS

EFISHG imaging is a powerful tool for visualizing transport in organic FETs. Not only is it relevant for probing the electric field within the channel, TR EFISHG, in particular, is an effective tool for obtaining contact-free and trap-free carrier mobilities. In the absence of any  $V_{DS}$ , the formation of the accumulation layer is discerned, which is directly related to the semiconductor-dielectric interface. We correlate the phenomenon of interface charging to the interface trap density and doping concentration as determined by  $C$ - $V$  and  $G$ - $V$  measurements.

In the area of organic electronics, there is a strong effort to improve the speed of organic FETs. Compared with MOSFETs and gallium-nitride high-electron mobility transistors, which routinely achieve  $R_c$  as low as  $0.01\Omega\text{ cm}$ , organic transistors typically show  $R_c$  in the range of  $100\text{ k}\Omega\text{ cm}$ , impeding the speed of organic FETs. Revisiting nonlinear optical imaging techniques for visualizing carrier transport in organic FETs has a lot of merit. Not only does TR EFISHG provide a mechanism for probing intrinsic carrier mobilities, the formation of the accumulation layer may also be visualized. By comparing a small molecule organic semiconductor with a donor-acceptor copolymer, and by systematically changing the gate dielectric, we find the discrepancy in carrier mobilities extracted from electrical measurements versus TR EFISHG is a result of the contact resistance of the device and the trapping of carriers. Moving forward, TR EFISHG measurements as a function of temperature could clarify the trends in carrier mobilities, highlighting activated versus bandlike transport in a specific semiconducting layer.

Capacitance and conductance measurements from  $M$ - $I$ - $S$  diodes helps in understanding the differences observed in the TR EFISHG images during interface-charging effect in pentacene/PMMA and DPP-DTT/PMMA FETs. A higher doping concentration in DPP-DTT is responsible for the fast formation of the accumulation layer, which is observed as a symmetric movement of the carrier wave front from both electrodes, conforming with the Maxwell-Wagner model. Further, the application of only an in-plane field maps the electric field and voltage inside the channel region. Not only do EFISHG images provide real-time measurement of carrier dynamics in organic FETs, they also reveal the impact of the semiconductor-dielectric interface on transport. An alternative way of measuring transport in organic FETs, as highlighted in this work, will provide future benchmark metrics for enhancing device performance.

### ACKNOWLEDGMENTS

We acknowledge the support of this work through the U.S. National Science Foundation under Grant No. ECCS-1872846 and ECCS-1707588. We thank John Barron for helping with the electrical measurements.

---

[1] H. Klauk, Will we see gigahertz organic transistors?, *Adv. Electron. Mater.* **4**, 1700474 (2018).  
 [2] A. Yamamura, S. Watanabe, M. Uno, M. Mitani, C. Mitsui, J. Tsurumi, N. Isahaya, Y. Kanaoka, T. Okamoto, and J. Takeya, Wafer-scale, layer-controlled organic single crystals for high-speed circuit operation, *Sci. Adv.* **4**, eaao5758 (2018).  
 [3] T. He, M. Stolte, Y. Wang, R. Renner, P. P. Ruden, F. Würthner, and C. D. Frisbie, Site-specific chemical doping

reveals electron atmospheres at the surfaces of organic semiconductor crystals, *Nat. Mater.* **20**, 1532 (2021).  
 [4] A. D. Scaccabarozzi, A. Basu, F. Anié, J. Liu, O. Zapata-Arteaga, R. Warren, Y. Firdaus, M. I. Nugraha, Y. Lin, M. Campoy-Quiles, N. Koch, C. Müller, L. Tsetseris, M. Heeney, and T. D. Anthopoulos, Doping approaches for organic semiconductors, *Chem. Rev.* **122**, 4420 (2022).  
 [5] D. He, J. Qiao, L. Zhang, J. Wang, T. Lan, J. Qian, Y. Li, Y. Shi, Y. Chai, W. Lan, L. K. Ono, Y. Qi, J.-B. Xu, W. Ji, and X. Wang, Ultrahigh mobility and efficient charge injection in monolayer organic thin-film transistors on boron nitride, *Sci. Adv.* **3**, e1701186 (2017).  
 [6] S. Fratini, M. Nikolka, A. Salleo, G. Schweicher, and H. Sirringhaus, Charge transport in high-mobility conjugated polymers and molecular semiconductors, *Nat. Mater.* **19**, 491 (2020).  
 [7] S. P. Senanayak, S. Guha, and K. S. Narayan, Polarization fluctuation dominated electrical transport processes of polymer-based ferroelectric field effect transistors, *Phys. Rev. B* **85**, 115311 (2012).  
 [8] N. Bloembergen, R. K. Chang, S. S. Jha, and C. H. Lee, Optical second-harmonic generation in reflection from media with inversion symmetry, *Phys. Rev.* **174**, 813 (1968).  
 [9] H. W. K. Tom, T. F. Heinz, and Y. R. Shen, Second-Harmonic Reflection from Silicon Surfaces and its Relation to Structural Symmetry, *Phys. Rev. Lett.* **51**, 1983 (1983).  
 [10] O. A. Aktsipetrov, A. A. Fedyanin, E. D. Mishina, A. N. Rubtsov, C. W. van Hasselt, M. A. C. Devillers, and T. Rasing, dc-electric-field-induced second-harmonic generation in Si(111)-SiO<sub>2</sub>-Cr metal-oxide-semiconductor structures, *Phys. Rev. B* **54**, 1825 (1996).  
 [11] O. A. Aktsipetrov, A. A. Fedyanin, A. V. Melnikov, E. D. Mishina, A. N. Rubtsov, M. H. Anderson, P. T. Wilson, M. ter Beek, X. F. Hu, J. I. Dadap, and M. C. Downer, dc-electric-field-induced and low-frequency electromodulation second-harmonic generation spectroscopy of Si(001)-SiO<sub>2</sub> interfaces, *Phys. Rev. B* **60**, 8924 (1999).  
 [12] J. I. Dadap, P. T. Wilson, M. H. Anderson, M. C. Downer, and M. ter Beek, Femtosecond carrier-induced screening of dc electric-field-induced second-harmonic generation at the Si(001)-SiO<sub>2</sub> interface, *Opt. Lett.* **22**, 901 (1997).  
 [13] J. Fang and G. P. Li, Detection of gate oxide charge trapping by second-harmonic generation, *Appl. Phys. Lett.* **75**, 3506 (1999).  
 [14] P. Godefroy, W. de Jong, C. W. van Hasselt, M. A. C. Devillers, and T. Rasing, Electric field induced second harmonic generation spectroscopy on a metal-oxide-silicon structure, *Appl. Phys. Lett.* **68**, 1981 (1996).  
 [15] D. Xiao, E. Ramsay, D. T. Reid, B. Offenbeck, and N. Weber, Optical probing of a silicon integrated circuit using electric-field-induced second-harmonic generation, *Appl. Phys. Lett.* **88**, 114107 (2006).  
 [16] T. Manaka, E. Lim, R. Tamura, and M. Iwamoto, Direct imaging of carrier motion in organic transistors by optical second-harmonic generation, *Nat. Photon.* **1**, 581 (2007).  
 [17] T. Manaka, E. Lim, R. Tamura, D. Yamada, and M. Iwamoto, Probing of the electric field distribution in organic field effect transistor channel by microscopic second-harmonic generation, *Appl. Phys. Lett.* **89**, 072113 (2006).

- [18] T. Manaka, F. Liu, M. Weis, and M. Iwamoto, Diffusionlike electric-field migration in the channel of organic field-effect transistors, *Phys. Rev. B* **78**, 121302 (2008).
- [19] D. Yamada, T. Manaka, E. Lim, R. Tamura, and M. Iwamoto, Probing of electric field in pentacene using microscopic optical second harmonic generation, *J. Appl. Phys.* **103**, 084118 (2008).
- [20] I. Mitsumasa, M. Takaaki, and T. Dai, Probing and modeling of carrier motion in organic devices by electric-field-induced optical second-harmonic generation, *Jpn. J. Appl. Phys.* **53**, 100101 (2014).
- [21] T. Manaka and M. Iwamoto, Optical second-harmonic generation measurement for probing organic device operation, *Light Sci. Appl.* **5**, e16040 (2016).
- [22] M. Weis, J. Lin, D. Taguchi, T. Manaka, and M. Iwamoto, The charge transport in organic field-effect transistor as an interface charge propagation: The Maxwell–Wagner effect model and transmission line approximation, *Jpn. J. Appl. Phys.* **49**, 071603 (2010).
- [23] M. Iwamoto and D. Taguchi, *Maxwell Displacement Current and Optical Second-Harmonic Generation in Organic Materials: Analysis and Application for Organic Electronics* (World Scientific, Singapore, 2021).
- [24] R. W. Boyd, *Nonlinear Optics* (Academic Press, Inc., London, 2020), 4th ed.
- [25] O. Ostroverkhova, A. Stickrath, and K. D. Singer, Electric field-induced second harmonic generation studies of chromophore orientational dynamics in photorefractive polymers, *J. Appl. Phys.* **91**, 9481 (2002).
- [26] R. L. Fork, O. E. Martinez, and J. P. Gordon, Negative dispersion using pairs of prisms, *Opt. Lett.* **9**, 150 (1984).
- [27] J.-C. Diels and W. Rudolph, *Ultrashort Laser Pulse Phenomena* (Elsevier, Burlington, 2006).
- [28] See Supplemental Material at <http://link.aps.org/supplemental/10.1103/PhysRevApplied.19.044059> for details on the experimental setup; absorption spectrum of DPP-DTT; electrical characteristics of pentacene and DPP-DTT FETs, TR EFISHG images from pentacene-SiO<sub>2</sub> FETs; capacitance characteristics from metal-insulator-semiconductor devices.
- [29] J. Barron, S. Attar, P. Bhattacharya, P. Yu, M. Al-Hashimi, and S. Guha, Visualizing transport in thiazole flanked isoindigo-based donor–acceptor polymer field-effect transistors, *J. Mat. Chem. C* **10**, 14653 (2022).
- [30] P. Sonar, S. P. Singh, Y. Li, M. S. Soh, and A. Dodabalapur, A low-bandgap diketopyrrolopyrrole-benzothiadiazole-based copolymer for high-mobility ambipolar organic thin-film transistors, *Adv. Mater.* **22**, 5409 (2010).
- [31] C. Kanimozhi, N. Yaacobi-Gross, K. W. Chou, A. Amasian, T. D. Anthopoulos, and S. Patil, Diketopyrrolopyrrole–diketopyrrolopyrrole-based conjugated copolymer for high-mobility organic field-effect transistors, *J. Am. Chem. Soc.* **134**, 16532 (2012).
- [32] H. W. Lee, H. S. Kim, D. Kim, M. Yoon, J. Lee, and D.-H. Hwang, Comparative study of charge-transport behavior of edge-on- and face-on-oriented diketopyrrolopyrrole-based conjugated copolymers bearing chalcogenophene units, *Chem. Mater.* **34**, 314 (2022).
- [33] T. Manaka, Y. Suzue, and M. Iwamoto, Investigation of the electrostatic phenomena at pentacene/metal interface by second-harmonic generation, *Jpn. J. Appl. Phys.* **44**, 2818 (2005).
- [34] Y. Lei, P. Deng, J. Li, M. Lin, F. Zhu, T.-W. Ng, C.-S. Lee, and B. S. Ong, Solution-processed donor-acceptor polymer nanowire network semiconductors for high-performance field-effect transistors, *Sci. Rep.* **6**, 24476 (2016).
- [35] I. N. Hulea, S. Fratini, H. Xie, C. L. Mulder, N. N. Iosad, G. Rastelli, S. Ciuchi, and A. F. Morpurgo, Tunable Fröhlich polarons in organic single-crystal transistors, *Nat. Mater.* **5**, 982 (2006).
- [36] A. Laudari and S. Guha, Polarization-induced transport in ferroelectric organic field-effect transistors, *J. Appl. Phys.* **117**, 105501 (2015).
- [37] A. Laudari and S. Guha, Temperature dependent carrier mobility in organic field-effect transistors: The role of dielectrics, *J. Appl. Phys.* **125**, 035501 (2019).
- [38] M. Waldrip, O. D. Jurchescu, D. J. Gundlach, and E. G. Bittle, Contact resistance in organic field-effect transistors: Conquering the barrier, *Adv. Funct. Mater.* **30**, 1904576 (2020).
- [39] Y. Xu, Y. Li, S. Li, F. Balestra, G. Ghibaudo, W. Li, Y.-F. Lin, H. Sun, J. Wan, X. Wang, Y. Guo, Y. Shi, and Y.-Y. Noh, Precise extraction of charge carrier mobility for organic transistors, *Adv. Funct. Mater.* **30**, 1904508 (2020).
- [40] O. J. Sandberg, M. Nyman, S. Dahlström, S. Sandén, B. Törngren, J.-H. Smått, and R. Österbacka, On the validity of MIS-CELIV for mobility determination in organic thin-film devices, *Appl. Phys. Lett.* **110**, 153504 (2017).
- [41] L. Bürgi, R. H. Friend, and H. Sirringhaus, Formation of the accumulation layer in polymer field-effect transistors, *Appl. Phys. Lett.* **82**, 1482 (2003).
- [42] E. H. Nicollian and J. R. Brews, *MOS (Metal Oxide Semiconductor) Physics and Technology* (Wiley, New York, 2003).
- [43] M. Yun, S. Gangopadhyay, M. Bai, H. Taub, M. Arif, and S. Guha, Interface states in polyfluorene-based metal–insulator–semiconductor devices, *Org. Electron.* **8**, 591 (2007).
- [44] S. Guha, D. Adil, N. B. Ukah, R. K. Gupta, and K. Ghosh, Maple-deposited polymer films for improved organic device performance, *Appl. Phys. A* **105**, 547 (2011).
- [45] K. Gooden, A. Laudari, G. Knotts, and S. Guha, Printed dielectric-based organic diodes and transistors, *Flex. Print. Electron.* **1**, 015004 (2016).
- [46] H. Sun, S. Ryno, C. Zhong, M. K. Ravva, Z. Sun, T. Körzdörfer, and J.-L. Brédas, Ionization energies, electron affinities, and polarization energies of organic molecular crystals: Quantitative estimations from a polarizable continuum model (PCM)-tuned range-separated density functional approach, *J. Chem. Theory Comput.* **12**, 2906 (2016).
- [47] D. Adil, C. Kanimozhi, N. Ukah, K. Paudel, S. Patil, and S. Guha, Electrical and optical properties of diketopyrrolopyrrole-based copolymer interfaces in thin film devices, *ACS Appl. Mater. Interfaces* **3**, 1463 (2011).
- [48] J. W. Borchert, R. T. Weitz, S. Ludwigs, and H. Klauk, A critical outlook for the pursuit of lower contact resistance in organic transistors, *Adv. Mater.* **34**, 2104075 (2022).

- [49] F. Chiarella, M. Barra, A. Carella, L. Parlato, E. Sarnelli, and A. Cassinese, Contact-resistance effects in PDI8-CN2 n-type thin-film transistors investigated by kelvin-probe potentiometry, *Org. Electron.* **28**, 299 (2016).
- [50] J. D. Morris, T. L. Atallah, C. J. Lombardo, H. Park, A. Dodabalapur, and X.-Y. Zhu, Mapping electric field distributions in biased organic bulk heterojunctions under illumination by nonlinear optical microscopy, *Appl. Phys. Lett.* **102**, 033301 (2013).